DOI: 10.1002/ejic.201000882

Structure and Conformational Properties of Azido(difluoro)phosphane, F_2PN_3

Xiaoqing Zeng,[a] Helmut Beckers,*[a] Helge Willner,[a] Raphael J. F. Berger,[b] Stuart A. Hayes,[b] and Norbert W. Mitzel[b]

Keywords: Azides / Vibrational spectroscopy / Electron diffraction / Conformation analysis / Ab initio calculations

Azido(difluoro)phosphane, F_2PN_3, is a colorless gas, which freezes to a glassy solid at ca. –120 °C, and the boiling point obtained by extrapolating the vapor-pressure curve is 8 °C. It has been characterized by IR (gas phase, Ar matrix), Raman (liquid, amorphous, and crystalline solid), and ^{19}F, ^{31}P, ^{14}N, and ^{15}N NMR spectroscopy. The conformational properties of F_2PN_3 have been studied by vibrational spectroscopy, gas electron diffraction (GED), and quantum chemical calculations. An almost equimolar mixture of two conformers was identified in the gas and neat liquid phases, as well as in Ar matrix, for which the N_3 group adopts a *syn* and *anti* orientation with respect to the bisector of the FPF angle. The *syn* conformer was found to be slightly more stable than the *anti* conformer by 2.4 ± 0.6 kJ mol^{-1} ($\Delta H°$) determined by gas–phase temperature-dependent IR spectroscopy, but in the crystalline state at low-temperature only the *anti* form is observed. The very different conformational properties of F_2PN_3 relative to that of the previously investigated F_2PNCO are discussed, guided by a natural bond orbital (NBO) analysis of electron delocalizations and steric exchange repulsions.

Introduction

Although the synthesis of main group azides is a challenge because of their hazardous properties, their chemistry is of general interest.[1] Especially, phosphinoyl azides with organic substituents, R_2PN_3, were shown to be versatile building blocks in phosphorus chemistry and have widely been used in the synthesis of oligomeric phosphazenes with repeating units $[–NPR_2–]_n$ through thermal or photolytic decomposition.[2] However, because of their low thermal stability, only a few phosphinoyl azides, stabilized by bulky electron-donating amino groups have been prepared and structurally characterized so far.[3]

The knowledge about phosphorus(III) azides X_2PN_3 (X = substituent more electronegative than phosphorus) is even more scarce. Only very few examples have been prepared and spectroscopically identified,[4] but their conformational and structural properties remain unknown. Azido(difluoro)phosphane, F_2PN_3, which was reported to be thermally and photolytically unstable and may occasionally explode spontaneously at room temperature, has been characterized by gas-phase IR and ^{19}F NMR spectroscopy and mass spectrometry.[5,6] Recently, the photo-induced decomposition of F_2PN_3 to $F_2P{\equiv}N$ and N_2 was studied in an Ar matrix, the initially formed $F_2P{\equiv}N$ further isomerizes to FP=NF.[7]

For alkoxy,[8] amino,[9] and primary phosphanes,[10] several different conformers with respect to the internal rotation around the $R_2P–X$ (X = OR, CR_3, and NR_2) bond have been established by vibrational spectroscopy and gas-phase electron diffraction (GED) studies. However, analogous experiments on the pseudohalide derivatives F_2PNCO, F_2PNCS,[11] and F_2PNCSe[12] revealed the existence of only one conformer, in which the pseudohalogen groups are in an antiperiplanar (*anti*) orientation with respect to the bisector of the FPF angle. To the contrary, in the previously reported gas-phase IR spectrum of F_2PN_3, two strong IR bands appear in the region of the symmetric N_3 stretching vibration (1230–1260 cm^{-1}).[6] This feature may indicate a different conformational behavior and the presence of two different conformers for F_2PN_3 in the gas phase.

Recently, we investigated the conformational properties of the related phosphoryl pseudohalides $F_2P(O)N_3$ and $F_2P(O)NCO$.[13] Their most-stable conformers adopt a coplanar *syn* orientation with respect to the P=O bond, which was rationalized by stereoelectronic as well as by dipole–dipole interactions between the phosphoryl and the pseudohalide moieties.[13] In this work, the spectroscopic and conformational properties of F_2PN_3 have been explored by using vibrational spectroscopy, GED, and quantum chemical calculations. The conformational behavior of previously investigated F_2PNCO, was found to be surprisingly unrelated to that of the title compound.

[a] Bergische Universität Wuppertal, FB C – Anorganische Chemie,
Gauß-Straße 20, 42097 Wuppertal, Germany
Fax: +49-202-439-3053
E-mail: beckers@uni-wuppertal
[b] Universität Bielefeld, Lehrstuhl für Anorganische Chemie und Strukturchemie,
Universitätsstraße 15, 33615 Bielefeld, Germany

Supporting information for this article is available on the WWW under http://dx.doi.org/10.1002/ejic.201000882.

Results and Discussion

Vibrational Analysis

IR frequencies (2200–600 cm^{-1}) for F_2PN_3 in the gas phase have already been reported but have not been completely assigned.[6] Our experimental IR (gas phase and matrix) and Raman (liquid, amorphous, and crystalline solid) spectroscopic data are collected in Table 1 and are compared to the calculated fundamental frequencies [B3LYP/6-311+G(3df)] for two different conformers of F_2PN_3. Observed bands are finally assigned to two different isomers, in which the N_3 group adopts either the *syn* or the *anti* position with respect to the bisector of the FPF angle, as shown in Figure 1.

The gas-phase IR spectrum of F_2PN_3 is shown in Figure 2. The N_3 asymmetric stretch (ν_1) is observed at 2153 cm^{-1} as the strongest band. Two overlapping bands with almost equal intensities appear in the region of the N_3 symmetric stretching vibration (ν_2) at 1268 and 1228 cm^{-1}, which indicates the presence of two different conformers. According to the calculated frequencies (Table 1), these two bands are assigned to the *anti* ($\nu_{calcd.}$ = 1352 cm^{-1}) and the *syn* forms ($\nu_{calcd.}$ = 1297 cm^{-1}), respectively. Support for this assignment stems from the assignment of their overtones $2\nu_2$ at 2523 cm^{-1} (*anti*) and 2432 cm^{-1} (*syn*).

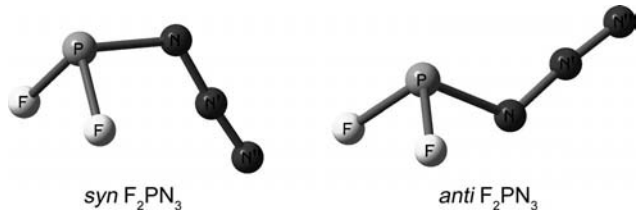

Figure 1. *syn* and *anti* conformers of F_2PN_3.

The well-resolved two overtone bands associated with the two conformers enable the study of their temperature-dependent conformational equilibrium in the gas phase. The IR spectra of gaseous F_2PN_3 at three temperatures between 294 and 214 K are shown in Figure 3 (for the complete set of the spectra recorded in this temperature range see Figure S1 in the Supporting Information). The relative intensity of the band at 2432 cm^{-1} increases at the expense of the band at 2523 cm^{-1} (which is normalized for comparison) as the temperature of the IR cell is lowered, which indicates a higher stability of the conformer (*syn*) associated with the former band.

Table 1. Experimental[a] and calculated[b] vibrational frequencies of F_2PN_3.

$IR_{exp.}$ Vapor (298 K)	Ar matrix (15 K)[c]	$Raman_{exp.}$ Liquid (298 K)	Amorphous solid (77 K)	Crystalline solid (143 K)	$IR_{calcd.}$[b]	Assignment/mode[d]
3411 vw						*anti*, $\nu_1 + \nu_2$
3346 vw						*syn*, $\nu_1 + \nu_2$
2895 vw						$\nu_1 + \nu_4$
2523 w						*anti*, 2 ν_2,
2432 w						*syn*, 2 ν_2
2153 vs	2148.1 vs				2279 (524)	*syn*, ν_1, $\nu_{as}(N_3)$
		2148 s, br.	2167 s, br.	2165 s	2278 (752)	*anti*, ν_1, $\nu_{as}(N_3)$
1484 w	1483.0 vw					*anti*, 2 ν_4
	1476.9 vw					*syn*, 2 ν_4
1268 s	1282.1 s	1270 m	1273 m	1272 m	1352 (235)	*anti*, ν_2, $vs(N_3)$
1228 s	1228.6 s	1231 w, sh.			1297 (334)	*syn*, ν_2, $vs(N_3)$
1206 sh.	1205.3 m					*syn*, 2 ν_5
1150 w	1150.8 w					*anti*, 2 ν_5
857 s	861.8 s	849 m, sh.		848 w	839 (197)	*anti*, ν_3, vs(PF)
831 s, br.	837.4 s	830 m	834 m, 807 m	821 s, 802 w	813 (163)	*anti*, ν_9, $\nu_{as}(PF)$
	831.4 s				808 (111)	*syn*, ν_3, vs(PF)
	803.8 s				779 (167)	*syn*, ν_9, $\nu_{as}(PF)$
743 s	742.9 s	732 s	735 m, br.	745 s, 751 m	727 (134)	*anti*, ν_4, ν(PN)
	739.9 s				729 (79)	*syn*, ν_4, ν(PN)
611 s	606.8 s	601 m			613 (163)	*syn*, ν_5, i.p. $\delta(N_3)$
	577.8 w				602 (9)	*syn*, ν_{10}, o.p. $\delta(N_3)$
	560.6 vw				588 (3)	*anti*, ν_{10}, o.p. $\delta(N_3)$
561 w	551.7 m	551 vs	547 vs	554 vs, 568 w	566 (67)	*anti*, ν_5, i.p. $\delta(N_3)$
447 w	447.7 w				439 (12)	*syn*, ν_6, $\delta(PF_2)$
	446.0 w	446 s	446 s	443 s	430 (11)	*anti*, ν_6, $\delta(PF_2)$
	350.3 w				337 (10)	*syn*, ν_7, $\omega(PF_2)$
	326.0 w	350 w, sh.	331 m	330 s	311 (7)	*anti*, ν_7, $\omega(PF_2)$
	313.8 vw				314 (2)	*syn*, ν_{11}
		327 m	318 w, sh.	318 w	296 (2)	*anti*, ν_{11}
		175 s	190 vs	204 s, 188 s	169 (2)	*anti*, ν_8
		143 m sh.			130 (1)	*syn*, ν_8
					57 (<1)	*syn*, ν_{12}
		82 s, br.	105 s, br.	104 m, 84 m	30 (<1)	*anti*, ν_{12}

[a] Experimental band positions and intensities: vs very strong, s strong, m medium strong, w weak, vw very weak, sh. shoulder, and br. broad. [b] B3LYP/6-311+G(3df) level; infrared intensities (km mol^{-1}) in parenthesis. [c] Most-intensive matrix site. [d] Approximate mode descriptions were made according to a C_s symmetry.

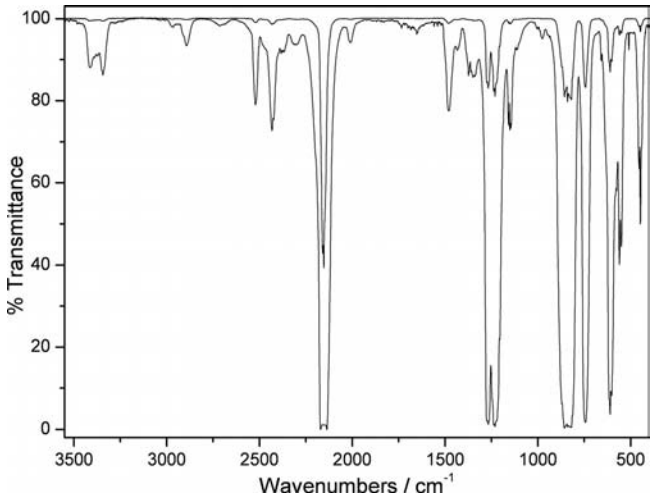

Figure 2. IR spectra of gaseous F_2PN_3 recorded at two different pressures of 1.0 and 13.0 mbar (optical path length 20 cm, 298 K).

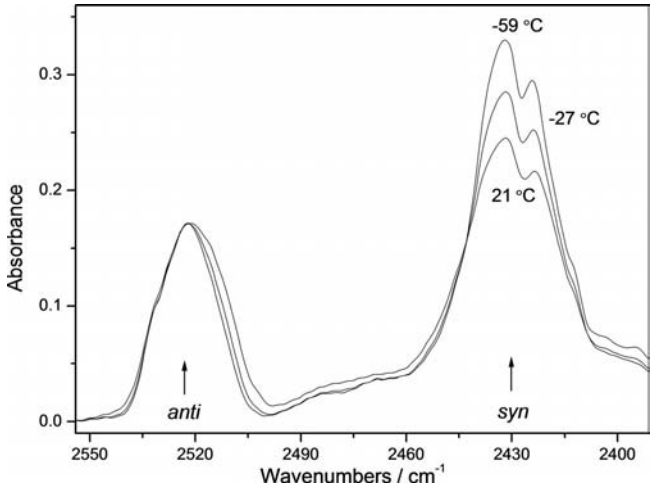

Figure 3. Temperature dependence of the IR bands at 2523 (normalized) and 2432 cm^{-1} assigned to *anti* and *syn* F_2PN_3, respectively.

The van't Hoff plot, $\ln(I_{anti}/I_{syn}) = -\Delta_{conf}H°/RT$ + constant, obtained from the temperature dependence of the integrated intensities I_{anti}/I_{syn} of $2\nu_2$ for the two conformers is shown in Figure 4. From this graph, the standard enthalpy difference ($\Delta H°$) for the *syn–anti* interconversion [Equation (1)] is determined to be 2.4 kJ mol^{-1}.

syn $F_2PN_3 \rightleftharpoons$ *anti* F_2PN_3 $\Delta H_R = 2.4 \pm 0.6$ kJ mol^{-1} (1)

By assuming an uncertainty of ±2 °C in the IR gas cell temperatures and ±2% in the integrated band areas, the uncertainty in the enthalpy difference ΔH_R is estimated to be ±0.6 kJ mol^{-1}. At room temperature, the Gibbs free energy difference $\Delta G° \approx 0.8 \pm 0.6$ kJ mol^{-1}, estimated from the experimental enthalpy difference ΔH_R and a calculated entropy difference of $\Delta S° = 5.4$ J mol^{-1} K^{-1} [B3LYP/6-311+G(3df)], corresponds to a concentration of 44 ± 6% *anti* F_2PN_3 in the gas phase.

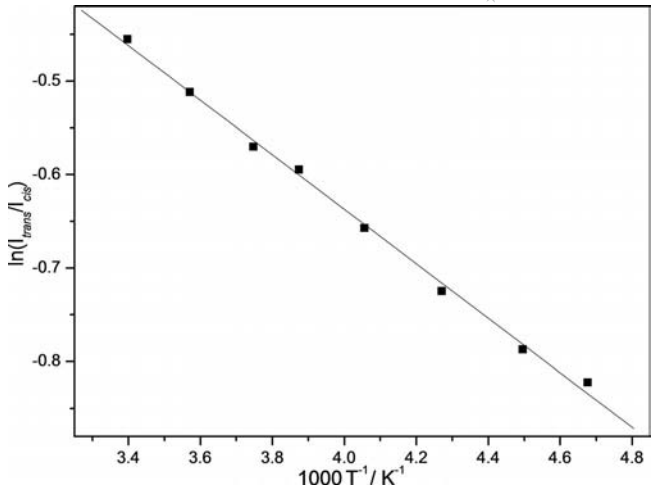

Figure 4. Van't Hoff plot obtained in the temperature range 294–214 K from the ratios of the integrated areas I_{anti}/I_{syn} of the $2\nu_2$ bands at 2523 and 2432 cm^{-1} (Figure 3) for *anti* and *syn* F_2PN_3, respectively.

The Raman spectra obtained from liquid (300 K) and solid (77 K) F_2PN_3 are very similar, although the bands observed from the amorphous solid (Figure S2) appear to be slightly sharper. A slow increase in the temperature of the solid from 77 to ca. 143 K causes a further sharpening of the bands, and finally a very well-resolved Raman spectrum of a crystalline solid was obtained (Figure 5, lower trace). Only one conformer contributes to the spectrum in the solid, which by comparison with the spectrum of Ar-matrix isolated F_2PN_3 (Figure 5, upper trace), and with the predicted band positions (Table 1) can be assigned to the *anti* conformer. The presence of the less-stable *anti* form in the solid state is surprising and can probably be explained by (i) the very small enthalpy difference between the two conformers and (ii) the larger calculated dipole moment of the *anti* form [B3LYP/6-311+G(3df): *anti* 1.10 D, *syn* 0.90 D; MP2/TZVPP: *anti* 1.51 D, *syn* 0.53 D], which might stabi-

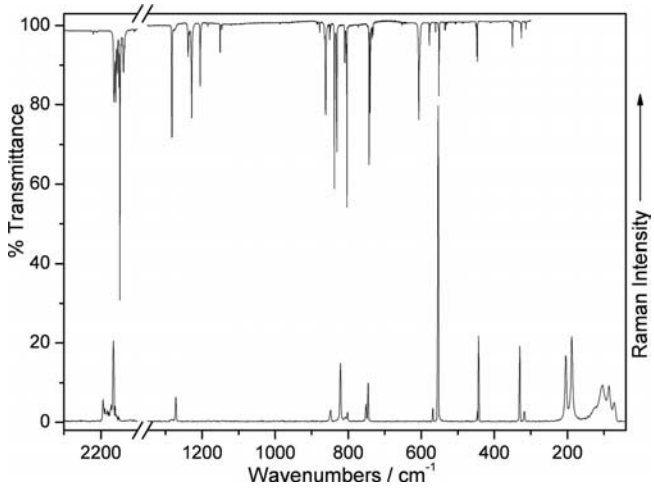

Figure 5. IR spectrum of F_2PN_3 isolated in solid argon at 15 K (upper trace) and Raman spectrum of crystalline F_2PN_3 at 143 K (lower trace).

lize *anti* F_2PN_3 through stronger intermolecular interactions. Such intermolecular interactions also account for the factor-group splitting of some of the major bands observed in the solid-state Raman spectra (Table 1 and Figure 5, lower trace).

All the Raman-active fundamental modes ($\Gamma_v = 8a' + 4a''$) are observed in the Raman spectrum of crystalline F_2PN_3, with the exception of the N_3 out-of-plane bending mode (ν_{10}), for which only a very low Raman activity is predicted. Relative to the solid-state spectra, the Raman spectra of the neat liquid reveal only three additional relatively weak and broad bands at 1231 (w), 601 (m), and 143 cm^{-1} (m), which can be attributed to the *syn* conformer. From their relative intensities, we conclude that the *anti* form also prevails in the liquid state.

The IR spectrum of Ar-matrix isolated F_2PN_3 (15 K) shown in Figure 5 (upper trace) displays only one strong band at 2148.1 cm^{-1}. This feature is consistent with the predicted close band positions for both conformers of the antisymmetric N_3 stretching band ν_1 (Table 1). The strong ν_1 band is often accompanied by several weaker bands, which might be assigned to combination bands or different matrix sites.[13]

The existence of two different conformers in the matrix-isolated sample is ascertained by the appearance of four strong PF_2 stretching bands in the region 900–800 cm^{-1}, while only two bands at 858.1 [$\nu_s(PF_2)$] and 839.4 cm^{-1} [$\nu_{as}(PF_2)$] are observed for F_2PNCO (which exists exclusively in the *anti* form, Figure S3). In addition, the N_3 symmetric stretching bands located at 1282.1 (*anti*) and 1228.6 cm^{-1} (*syn*) and the P–N stretch at about 740 cm^{-1} are split into doublets because of the presence of two different conformers. To distinguish between the IR spectra of the two conformers, matrix deposition of gaseous F_2PN_3/Ar (1:500) mixtures was performed by passing them through a heated spray-on nozzle. The azide diluted in Ar shows no decomposition even at nozzle temperatures of up to 410 °C. The spectral changes obtained in the mid-infrared region at two different nozzle temperatures of 25 °C and 200 °C are displayed in Figure 6. These experiments provide an independent assignment of the two sets of bands associated with the two different conformers. As shown in Figure 6, upon heating the mixture, the ν_2 band observed at 1282.1 cm^{-1} increases in intensity at the expense of the corresponding band at 1228.6 cm^{-1}, and the observed frequency shift (53.5 cm^{-1}) between them agrees with the calculated difference (55 cm^{-1}) between the *anti* and *syn* conformers. Thus, the relative greater stability of the *syn* conformer vs. the *anti* conformer is further proven by a sudden trapping of the gas-phase equilibrium mixture, and the portion of the energetically less stable *anti* conformer is increased by heating the gaseous mixture prior to matrix isolation. Although the internal rotational barrier about the P–N bond is calculated to be less than 9 kJ mol^{-1} at the B3LYP/6-311+G(3df) level of theory, attempts to interconvert the conformers by annealing the matrix in the temperature range 10–33 K failed, and only the less-stable matrix sites decrease in intensity upon annealing.

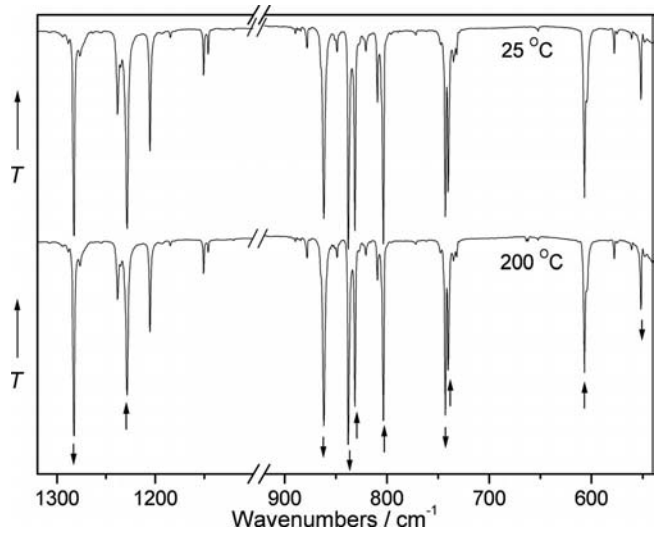

Figure 6. Expanded view of the Ar-matrix IR spectra (1320–1100 cm^{-1} and 920–540 cm^{-1}, transmittance *T*) of F_2PN_3 (F_2PN_3/Ar = 1:500) recorded at two different nozzle temperatures of 25 °C (upper trace) and 200 °C (lower trace). Downward and upward arrows indicate increasing and decreasing intensities, respectively, of the associated bands upon heating.

From the integrated intensities of the well-separated components of ν_2, ν_3, ν_4, ν_5, ν_9, and ν_{10} for the *syn* and *anti* conformers, the relative amounts of the two conformers of F_2PN_3 in solid Ar are estimated by using calculated absorption cross sections. This method yields an average content of 43% *anti* conformer in the Ar-matrix isolated sample (Table S1), which is very close to the concentration of 44 ± 6% at room temperature as determined by temperature-dependent gas-phase IR measurements. This observation indicates that the relative composition of the two conformers remains nearly unchanged during matrix deposition.

Further proof for the assignments of the IR bands to the two conformers came from ^{15}N-isotopic labeling experiments. The $^{14/15}N$ isotopic shifts of the bands in the region 1320–540 cm^{-1} show distinct conformational dependence (Figure S4), and the observed shifts $\Delta\nu^{14/15}N$ for $F_2PNN'^{15}N''$ and $F_2P^{15}NN'N''$ are in good agreement with the calculated data for the *syn* and *anti* conformers collected in Tables 2 and 3, respectively. The very small $^{14/15}N$ isotopic shifts for the PF_2 stretches (ν_3 and ν_9)

Table 2. Calculated[a] and experimental[b] isotopic shifts of *syn* F_2PN_3.

Assignment	$\Delta\nu^{14/15}N''$[c]		$\Delta\nu^{14/15}N$[d]	
	calcd.	exp.	calcd.	exp.
ν_2	11.3	8.5	29.7	29.6
ν_3	0.2	0.0	0.1	0.1
ν_4	1.6	1.4	14.3	15.2
ν_5	2.5	2.4	0.5	0.6
ν_9	0.0	0.0	0.0	0.0
ν_{10}	3.4	3.1	3.8	3.8

[a] B3LYP/6-311+G(3df) method. [b] Ar matrix. [c] Isotopic shifts of $F_2PNN'^{15}N''$ relative to F_2PN_3. [d] Isotopic shifts of $F_2P^{15}NN'N''$ relative to F_2PN_3.

indicate their negligible coupling to the P–N stretching vibration, while a weak coupling between $\nu_s(N_3)$ (ν_2) and ν(PN) (ν_4) can be deduced from the substantial shift of ν_4 upon ^{15}N substitution of the terminal N′′ atom. An expanded view of the matrix IR spectrum of mono-^{15}N labeled F_2PN_3 in the range 760–540 cm^{-1} is shown in Figure 7. The close-lying in-plane (i.p., ν_5) and out-of-plane (o.p., ν_{10}) bending modes of the azide group at about 600 cm^{-1} are easily distinguished by their $^{14/15}N$ isotopic shifts, particularly with ^{15}N labeling at the α-nitrogen position.

Table 3. Calculated[a] and experimental[b] isotopic shifts of *anti* F_2PN_3.

Assignment	$\Delta\nu^{14/15}N''$[c]		$\Delta\nu^{14/15}N$[d]	
	calcd.	exp.	calcd.	exp.
ν_2	13.2	10.6	30.7	28.0
ν_3	0.0	0.4	0.6	0.5
ν_4	1.2	1.0	13.1	13.6
ν_5	2.7	2.6	0.5	0.2
ν_9	0.0	0.1	0.0	0.1
ν_{10}	3.9	3.7	2.1	1.9

[a] B3LYP/6-311+G(3df) method. [b] Ar matrix. [c] Isotopic shifts of $F_2PNN'^{15}N''$ relative to F_2PN_3. [d] Isotopic shifts of $F_2P^{15}NN'N''$ relative to F_2PN_3.

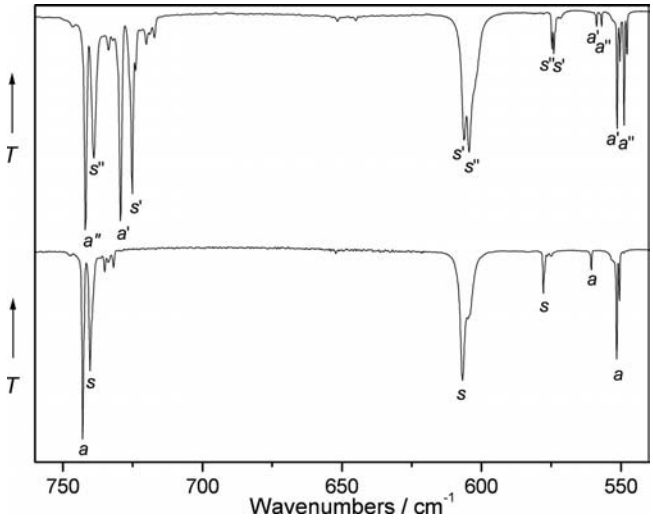

Figure 7. Expanded view of the Ar-matrix IR spectra (760–540 cm^{-1}, transmittance T) of F_2PN_3 (lower trace) and of a 1:1 mixture of $F_2P^{15}NNN$ and $F_2PNN^{15}N$ (upper trace). Bands labeled with *s*/*a*, *s*′/*a*′, and *s*′′/*a*′′ belong to *syn*/*anti* F_2PN_3, $F_2P^{15}NNN$, and $F_2PNN^{15}N$, respectively.

Gas-Phase Structure

According to the spectroscopic and quantum chemical results, a model with two C_s symmetric conformers, *syn* and *anti*, was used for the structure-refinement procedure. As the calculated vibrational normal modes and frequencies show (at the MP2/TZVPP level of theory, a frequency of 20 cm^{-1} is obtained for ν_{12} of *anti* F_2PN_3), a large amplitude motion for the N–*N*′–N′′ moiety in the *anti* conformer is expected. This expectation is confirmed by the broad feature in the radial distribution curve between 4 and 5 Å (Figure 8), which can be assigned to the F···N′′ distances from the *anti* conformer.

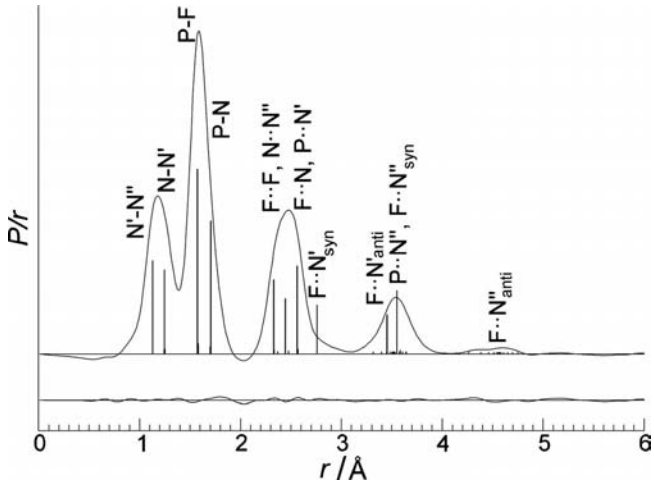

Figure 8. Radial distribution curve, difference (experimental minus theoretical) curve, and model from the GED structure refinement of F_2PN_3; the vertical sticks represent the interatomic distances (selected important ones are labeled).

Twelve degrees of freedom would have to be considered, for the description of the molecular geometry of each of the two conformers (3×6–6 = 12). However, the C_s symmetry reduces the number of degrees of freedom to nine, and the torsion angle τ(PN–N′N′′) to either 0 or 180° (this torsion angle is defined as an orientation of the N_3 unit relative to the "lone pair of electrons" at phosphorus in the plane of symmetry. Note that linearity was not assumed for the N–*N*′–N′′ moiety). The remaining eight molecular parameters estimated for the two conformers are listed in Table 4.

The large torsional motion of the azide group in the *anti* conformer, associated with the normal mode ν_{12} and τ_2 in Figure S5, was modeled by using nine equally weighted pseudoconformers *anti*(*i*) (*i* = 1,…,9) with different angles, $\tau_2 = \tau_{2,max}\,(i^2 - 1)/(80)$ ranging from 0° to a maximum angle $\tau_{2,max}$ and with increasing incremental angle differences. The maximum angle $\tau_{2,max}$ was refined as an independent parameter. In this way, a monotonically decreasing population density of τ_2 is modeled without further assumptions on the underlying potential or state population.

A total of 17 parameters are fitted in the least-squares refinement (a full list of independent and dependent parameters as well as amplitudes of vibration is provided in Tables S2–S8). Instead of refining two independent sets of eight structure parameters for both conformers, averages of the *anti*–*syn* differences were defined and used for each of the corresponding parameters. Flexible restraints in the sense of the established SARACEN[14] procedure were applied to these differences listed in Table 4. The interatomic amplitudes of vibration were partitioned into 9 groups according to the atom-pair distances involved. The relative ratio of the amplitudes of each of these groups were kept constant at the values calculated by the program SHRINK,[15] on the basis of a harmonic force field analysis

Table 4. Selected GED[a] and ab initio calculated[b] structural parameters of *syn* and *anti* F_2PN_3.

Parameters[c]	*syn* F_2PN_3 GED	HF	MP2	CAS[d]	*anti* F_2PN_3 GED	HF	MP2	GED restraints *anti* – *syn*
r(P–F)	1.579(1)	1.561	1.586	1.563	1.572(2)	1.546	1.575	–0.013(5)
r(P–N)	1.710(3)	1.679	1.709	1.670	1.716(3)	1.693	1.720	0.012(5)
r(N–N′)	1.250(3)	1.240	1.234	1.254	1.247(3)	1.230	1.230	0.002(5)
r(N′–N′′)	1.125(3)	1.080	1.150	1.102	1.127(3)	1.083	1.151	–0.007(5)
∠(FPF)	95.9(3)	95.2	96.5	94.9	96.4(2)	96.4	96.9	1.0(5)
∠(PNN′)	118.3(4)	119.3	119.8	118.6	117.7(5)	117.2	120.3	–1.3(5)
∠(NN′N′′)	178(1)	176.1	174.7	175.2	177(1)	176.3	174.7	–0.5(5)
τ(FP–NN′)	48.4(1)	48.8	48.6	48.7	131.5(2)	132.2	130.8	

[a] The GED results were determined by using the r_{h1} structure model. Restraint *anti* – *syn* differences and their uncertainties (in parentheses) applied in the refinement of the two-conformer model are listed in the last column. [b] The TZVPP basis set was used throughout. [c] Bond lengths (Å) and angles (°). [d] 4 electrons in 4 active orbitals (π → π*).

at the B3LYP/6-311G(3df) level of theory. In this calculation, the v_{12} mode of the *anti* conformer was excluded from the Hessian since this mode is modeled by using the pseudoconformers. The nine independent amplitudes were restrained to the calculated ones, by assuming an uncertainty of 10% of the calculated values. Some of the determined parameter differences are strongly correlated to interatomic vibrational amplitudes (see correlation matrix elements in Table S8). Hence, there is a comparably large uncertainty in some of the refined amplitudes and in the difference parameters.

The relative weights of the *syn* conformer and the set of nine *anti*(*i*) pseudoconformers were used as unrefined parameters, which were optimized with respect to the fit to the experimental scattering data in a separate step prior to the final structure–parameter refinement and were fixed in the refinement to those values that led to a minimum in the *R* factor R_G. This evaluation of the GED data results in a ratio of 48(5)% of the *syn* conformer, which corresponds to $\Delta G° = –0.2(5)$ kJ mol^{-1} at room temperature. This is in good agreement with the estimation of 0.8 ± 0.6 kJ mol^{-1}, which results from combined spectroscopic and quantum chemical results, bearing in mind that the accuracy of the total energy arising from first principles calculations is usually in the range of 5 kJ mol^{-1} at most.

The P–N bond length (r_{h1} value) obtained for the *syn* form of F_2PN_3 [1.710(3) Å] is shorter than that of the *anti* form [1.716(3) Å] by 0.006 Å. However, both bond lengths are much longer than the corresponding values of the related molecules F_2PNCO [1.683(6) Å], F_2PNCS [1.687(7) Å], and F_2PNCSe [1.649(12) Å] as determined by GED.[11,12] These pseudohalides also show substantial shorter P–F bond lengths, F_2PNCO [1.563(3) Å], F_2PNCS [1.566(3) Å], and F_2PNCSe [1.530(4) Å],[11,12] than those in F_2PN_3 [*syn*: 1.579(1) Å, *anti*: 1.572(2) Å]. The later ones are similar to that of F_2PCl [1.571(3) Å, microwave spectroscopy],[16] but significantly shorter than those in F_2PNH_2 [1.587(4) Å].[17]

Quantum Chemical Calculations

Structural parameters for the two C_s symmetric conformers of F_2PN_3 determined with ab initio HF and MP2 calculations are listed in Table 4 together with the results of the GED analysis; the calculated structures obtained by using DFT (B3LYP, BP86, MPW1PW91) and CBS-QB3 methods are given in Table S9. In general, there is good agreement between the GED structure parameters and the respective computational values. With the exception of the angle of the azide group, ∠(NN′N′′), the experimental parameters are within the expected range predicted at the HF and the MP2 levels (slightly closer to MP2).

Since the significant bond-length difference between the HF and MP2 values for the formally triple bonded N′–N′′ atoms (Table 4) might be a hint for a formal multiconfiguration character of the ground state wave function, a complete active space (CAS) multiconfigurationally self-consistent field (MCSCF) calculation was carried out for *syn* F_2PN_3. Formal excitation of 4 electrons from the two occupied π-type HF orbitals of the azido group into the corresponding unoccupied π*-type orbitals was allowed (4 electrons in 4 orbitals), which resulted in a total of 36 configuration state functions in the CAS calculation. Relative to the single reference HF configuration, the total energy dropped by 215.8 kJ mol^{-1}. The contribution of the latter one to the total CAS-MCSCF wave function is 89.5%, while a second configuration contributes about 2.6%. Obviously, the CAS-MCSCF calculation improves the N′–N′′ distance in question from 1.080 (HF) to 1.102 Å (CAS), relative to the experimental value of 1.125(3) Å (GED, vide infra). On the other hand, the MP2 calculation overestimates the N′–N′′ distance (1.150 Å), which indicates a certain (small) contribution of static correlation. However, the effects are small and the CAS calculation affects the other structural parameters only negligibly. We conclude that F_2PN_3 is a borderline case of a multireference ground state wave function, which is also in agreement with the good performance of the DFT methods in predicting the molecular structure.

The presence of an almost 1:1 mixture of two different conformers of F_2PN_3 in the gas phase at room temperature contrasts the known behavior of the related pseudohalides F_2PNCO, F_2PNCS, and F_2PNCSe, which exclusively exist in their *anti* forms.[11,12] These experimental results are fully verified at the DFT B3LYP/6-311+G(3df) level of theory. A potential energy scan over the τ(FP–NN) dihedral angle of

F_2PN_3 performed at this level reveals two minima, which correspond to the experimentally observed *syn* and *anti* conformers (Figure 9). These two conformers were confirmed to be true minima by using various ab initio (HF, MP2), DFT (B3LYP, BP86, MPW1PW91), and CBS-QB3 methods. Although their relative energy varies slightly with different applied methods, calculated energy differences are generally lower than 2.0 kJ mol^{-1} (Table S10). The transition state connecting the *syn* and *anti* conformers has been fully optimized at the B3LYP/6-311+G(3df) level and verified by an intrinsic reaction path calculation (IRC). It lies 4.6 kJ mol^{-1} in energy above the *anti* conformer and adopts a torsion angle τ(FP–NN) of 26.5°. An analogous energy scan performed for the related F_2PNCO yields only one minimum, namely the C_s symmetric *anti* conformer (Figure 9), which is consistent with the previous GED study on F_2PNCO.[11] The structures of the *syn* and *anti* conformers of F_2PNCO have been optimized by using different DFT methods (Table S11), and for all of the methods considered, the *syn* is always found to have an imaginary frequency.

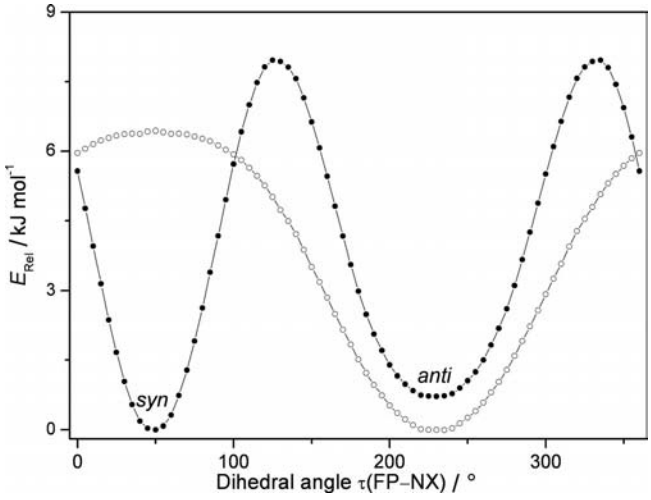

Figure 9. Potential energy scan over the dihedral angles τ(FP–NX) of F_2PN_3 (X = N, full circles line) and F_2PNCO (X = C, open circles) calculated at the B3LYP/6-311+G(3df) level of theory.

The competitive stability of *syn* F_2PN_3 is unexpected, as this conformer is expected to be disfavored by steric demand and repulsive phosphorus–nitrogen lone pair interaction. To provide insight into the origin of the *syn*-stabilizing interactions, we performed a comparative natural bond orbital (NBO) energetic and steric analysis[18] for the two related molecules F_2PN_3 and F_2PNCO. The default NBO Lewis-type structures obtained for the related molecules F_2PN_3 and F_2PNCO are very similar, which can be described for the azide by structure **A** in Scheme 1. According to the NBO description, in addition to the phosphorus σ-type lone pair n_σ(P), there are two lone pairs located on the α-nitrogen atom [denoted below by n_σ(N) and n_π(N)]. Because of symmetry restrictions, the out-of-plane lone pairs n_π(N) are composed of an almost pure nitrogen p-type atomic orbital, but substantial differences exist between the in-plane n_σ(N) lone pair NBOs of F_2PN_3 and F_2PNCO, as these correspond to sp-type (53.4 and 56.2% s-character in *syn* and *anti* F_2PN_3) and almost pure p-type nitrogen lone pairs (F_2PNCO), respectively. The different sp-hybridization of n_σ(N) accounts for the major structural differences of the two molecules, such as large variations between the angles at their α-N atoms and their P–N bond lengths (see Tables 4 and S11). These structural differences arise because the p-type nitrogen lone pairs are stronger donors than the sp-type lone pairs. The strongest lone pair–antibonding orbital (σ*) interactions for F_2PN_3 and F_2PNCO are observed between the nitrogen p-type lone pairs and the vicinal N≡N and C≡O triple bonds, respectively. Thus, with two nearly equally strong p-type n(N) → σ*(CO) interactions, the P–NCO moiety can be regarded as a "pseudo-linear" unit. To the contrary, the single p-type n_π(N) → σ*(N′N′′) delocalization in F_2PN_3 corresponds to the **A** ↔ **B** resonance description in Scheme 1.

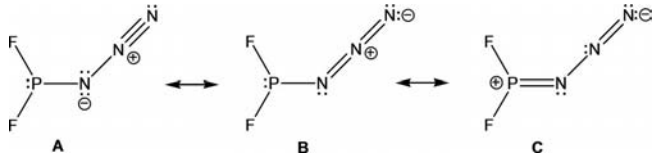

Scheme 1. Lewis resonance structures for F_2PN_3.

The conformational properties of the two pseudohalides are expected to be determined by a subtle balance between lone pair hyperconjugation effects, steric exchange repulsion, and probably other forces, such as dipole–dipole and electrostatic interactions. Contributions to the relative energy of a certain conformer from either stabilizing lone pair delocalization or various repulsive steric exchange bond orbital interactions can be adequately assessed by NBO second-order perturbation theory energies or natural steric analyses, respectively. These were carried out as single-point energy calculations at the fully optimized B3LYP/6-311+G(3df) geometry. A comprehensive account of the computational results for the two isomers of F_2PN_3 and F_2PNCO is given in the Tables S12 and S13 (second-order perturbation analysis) and Tables S14 and S15 (natural steric analysis), respectively.

As expected, the large stabilization energies observed for n_π(N) delocalization within the pseudohalide moieties by far exceed the contributions from n_π(N) → σ*(PF) hyperconjugation (Table 5). As shown in Table 5, the former interaction reveals a quite unexpected conformational dependence, as it strongly contributes to the relative stabilization of the *anti* conformation. As an additional consequence of the unequal hybridization of the σ-type n_σ(N) lone pairs at the *α*-nitrogen atom, its delocalization contributes very different to the conformational equilibrium of the studied compounds, e.g.: n_σ(N) → σ*(PF) hyperconjugation strongly favors the *syn* conformation of F_2PNCO by 45.9 kJ mol^{-1}, while this interaction stabilizes the *anti* form of F_2PN_3 by 29 kJ mol^{-1} (Table 5).

We note that for F_2PNCO, steric exchange repulsion favors the less stable *syn* conformer (Table S15), while the total NLMO steric exchange energies for the two rotamers of

Table 5. Main NBO delocalization interaction energies $E(2)$ and steric exchange repulsion energies $E(i,j)$ for the *syn* and *anti* conformers of F_2PN_3 and F_2PNCO.[a]

	$E(2)$ / kJ mol^{-1}[b]				$E(i,j)$ / kJ mol^{-1}[c]		
	syn	*anti*	*syn* – *anti*		*syn*	*anti*	*syn* – *anti*
F_2PN_3							
$n_\pi(N) \rightarrow \sigma^*(N'N'')$	433.5	462.5	–29.1	$n_\sigma(P)/n_\sigma(N)$	38.6	–2.3	40.9
$n_\pi(N) \rightarrow \sigma^*(PF)$[d]	64.2	55.9	8.3	$n_\sigma(N)/n_\sigma(F)$[d]	<2.0	19.1	ca. – 19.1
$n_\sigma(N) \rightarrow \sigma^*(PF)$[d]	7.3	36.2	–29.0	$n_\sigma(P)/\sigma(N'N'')$	<2.0	9.5	ca. – 9.5
$n_\sigma(P) \rightarrow \sigma^*(NN')$	21.1	< 2.0	ca. 21.1	$\sigma(PN)/\sigma(N'N'')$	46.9	56.4	– 9.5
$\sigma(PF) \rightarrow \sigma^*(PN')$[d]	28.3	9.8	18.5				
F_2PNCO							
$n_\pi(N) \rightarrow \sigma^*(CO)$	555.7	574.8	–19.0	$n_\sigma(P)/n_\sigma(N)$	–4.9	56.2	– 61.1
$n_\pi(N) \rightarrow \sigma^*(PF)$[d]	62.3	58.2	4.0	$n_\sigma(N)/n_\sigma(F)$[d]	22.3	<2.0	ca. 22.3
$n_\sigma(N) \rightarrow \sigma^*(CO)$	343.0	376.2	–33.2	$n_\sigma(N)/\sigma(PF)$[d]	51.8	<2.0	ca. 51.8
$n_\sigma(N) \rightarrow \sigma^*(PF)$[d]	60.1	14.1	45.9	$n_\sigma(F)/\sigma(PN)$[d]	30.0	48.5	– 18.5
$n_\sigma(N) \rightarrow \sigma^*(PN)$	63.5	91.3	–27.8				
$n_\sigma(P) \rightarrow \sigma^*(NC)$	32.3	6.5	25.9				

[a] Energies ≥ 2.0 kJ mol^{-1} obtained at the B3LYP/6-311+G(3df) optimized geometry. [b] Second-order perturbative estimates of hyperconjugative interaction (stabilization energy). [c] Steric exchange repulsion interaction (destabilization energy) of individual orbital pairs (i,j). [d] Values are doubled because two sets of the same interactions exist.

F_2PN_3 are well balanced (Table S14). These results suggest that steric repulsion might not be the essential factor of the *syn*–*anti* energetic differences in the two studied compounds. A converse behavior is, however, found for the repulsive $n_\sigma(P)/n_\sigma(N)$ exchange interaction, which stabilizes the *syn* conformation of F_2PNCO, but is *anti*-stabilizing in F_2PN_3 (Table 5).

For F_2PN_3, the major *syn*-stabilizing interaction is the phosphorus lone pair delocalization $n_\sigma(P) \rightarrow \sigma^*(NN')$. This interaction increases the electron density in the P–N bond at the expense of the strength of the adjacent N–N′ bond, as indicated by the Lewis representation **C** shown in Scheme 1. The corresponding stabilization energy for *anti*-F_2PN_3 is lower than the threshold printing (2 kJ mol^{-1}). The large conformational asymmetry of the $n_\sigma(P) \rightarrow \sigma^*(NN)$ delocalizations is depicted in Figure 10, where the overlap of the involved lone pair/antibonding NBOs for *syn* and *anti* F_2PN_3 are shown in the P–N–N′ plane. The plotted orbitals are pre-orthogonal PNBOs, and the overlap of the orbitals reflects the strength of the associated NBO Fock matrix elements. It should be noted that for *anti*-F_2PN_3 the like-phase overlap is nearly cancelled by an opposite-phase overlap (Figure 10). Further orbital contour plots for various vicinal lone pair–antibonding interactions discussed in Table 5 are shown in Figure S6.

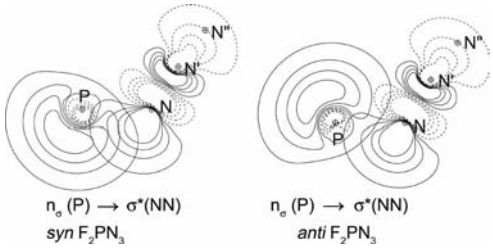

Figure 10. Orbital contour plots of the vicinal $n_\sigma(P) \rightarrow \sigma^*(NN)$ interactions in *syn*- and *anti*-F_2PN_3 obtained on the basis of the B3LYP/6-311+G(3df)-calculated structure. Plotted orbitals are pre-orthogonal PNBOs. Projections on the plane are defined by the various atoms shown in the plots.

Conclusions

The conformational equilibrium of *syn* and *anti* F_2PN_3 has been studied by gas-phase and Ar-matrix isolation vibrational spectroscopy, as well as by gas electron diffraction (GED). At room temperature these studies reveal an almost equimolar mixture of both conformers, where the *syn* conformer is found to be slightly more stable than the *anti* form by 2.4 ± 0.6 kJ mol^{-1} ($\Delta H°$) determined by gas-phase temperature-dependent IR spectroscopy. The experimental results are fully verified by theoretical calculations, but strongly contrast the known behavior of the related pseudohalide F_2PNCO, which exclusively exists in its *anti* form.[11]

As the conformational preferences of F_2PN_3 and F_2PNCO are difficult to predict, a NBO analysis has enlightened major contributions to the *syn*–*anti* energetic differences in these two compounds. It is not expected that estimates of the delocalization energies on a perturbative level and of steric exchange energies derived from pre-NLMO overlaps at the HF level might quantitatively account for the complicated conformational balance of these two compounds; however, in view of the NBO analysis, their different behavior can be attributed to the largely different hybridization of the σ-type lone pairs at the α-nitrogen atoms. This is found to be of almost pure p-type character in F_2PNCO, but of the sp-type in F_2PN_3. The significant differences in the gas-phase structures of F_2PN_3 and F_2PNCO, namely much longer P–N bond lengths and smaller bond angles at the α-nitrogen atom in F_2PN_3 [*syn*: 1.710(3) Å, 118.3(4)°; *anti*: 1.716(3) Å, 117.7(5)°] than the corresponding values in F_2PNCO [1.683(6) Å, 130.6(8)°],[11]

support this view. With two p-type lone pairs at a two-coordinate nitrogen atom, the PNCO skeleton in F_2PNCO might be viewed as "pseudolinear". The different delocalization behavior of $n_\sigma(N)$ in the two compounds appears to be crucial for understanding the different structural and conformational properties of the two compounds.

The most interesting and contrasting result of the NBO analysis is probably the large contribution from the $n_\sigma(N) \rightarrow \sigma^*(CO)$ delocalization to the conformational equilibrium in F_2PNCO, which strongly disfavors the unobserved *syn* conformation by 33.2 kJ mol^{-1} (Table 5). To the contrary, in F_2PN_3 the corresponding $n_\sigma(N) \rightarrow \sigma^*(N'N'')$ interaction is slightly *syn*-stabilizing (2.5 kJ mol^{-1}, Table S12). The importance of dipolar interactions, at least, of the intermolecular type was verified by solid-state Raman spectroscopy, which shows that in crystalline F_2PN_3, only the less-stable *anti* conformer exists.

Experimental Section

Caution! Covalent azides are, in general, explosive. Although we experienced no explosions with F_2PN_3 during this work, it should be prepared in less than millimolar quantities, and appropriate safety precautions should be taken especially when working with liquid F_2PN_3.

General Procedure and Reagents: Volatile materials were manipulated in a glass vacuum line equipped with a capacitance pressure gauge (221 AHS-1000, MKS Baratron, Burlington, MA) and three U-traps with PTFE valves (Young, London, U.K.). The vacuum line was connected to an IR cell (optical path length 20 cm, 0.5-mm thick Si windows), contained in the sample compartment of a Bruker Vector 25 FTIR spectrometer. The samples were purified by trap-to-trap condensation and stored in flame-sealed glass ampoules under liquid nitrogen in a long-term Dewar vessel. An ampoule was opened with an ampoule key[19] attached to the vacuum line, an appropriate amount was taken out, and then the ampoule was flame sealed again. F_2PCl[20] was prepared by the reaction of HCl with Et_2NPF_2,[21] F_2PNCO[22] from F_2PCl and AgOCN, and F_2PN_3[6] from F_2PCl and NaN_3 in toluene and was purified by vacuum trap-to-trap condensation. For the preparation of ^{15}N-labeled F_2PN_3, 1–^{15}N sodium azide (98 atom-% ^{15}N, EURISOTOP GmbH) was used as received. The purity of the products was checked by IR and NMR spectroscopy.

Instrumentation

Vibrational Spectroscopy: Temperature-dependent IR spectra of gaseous samples in the range –59 to 21 °C were recorded on the Bruker IFS 66v FTIR spectrometer employing a resolution of 2 cm^{-1}, by using a KBr beam splitter and a MCT detector. A double-walled gas cell with an optical path length of 20 cm was used, equipped with silicon windows (0.5 mm thick) and a pressure gauge (221 AHS-100, MKS Baratron, Burlington, MA). A Pt-100 temperature sensor was placed at the cell inside the evacuated sample chamber of the spectrometer. The temperature was controlled by adjusting the flow rate and temperature of a cold stream of nitrogen gas. For each temperature, a new background was measured, and the cell was filled with a new sample (ca. 10 mbar) from the F_2PN_3 reservoir.

Raman spectra were recorded on a Bruker-Equinox 55 FRA 106/S FT-Raman spectrometer by using a 1064 nm Nd:YAG laser (200 mW). A liquid sample was flame-sealed in a glass tube (o.d. 4.0 mm, i.d. 3.0 mm, length ca. 50 mm), and 100 scans were recorded at a resolution of 1 cm^{-1}. For low-temperature Raman measurements of solid samples, F_2PN_3 was condensed under high vacuum onto a copper finger cooled with liquid nitrogen. An amorphous/glassy solid was first obtained, and the Raman bands were similar to those of the liquid. Upon annealing to ca. –130 °C, all bands became very sharp and some bands disappeared. Attempts to grow single crystals by in situ crystallization on an X-ray diffractometer failed.

Gas Electron Diffraction: The electron diffraction patterns were recorded with a modified KD-G2 gas diffractometer at the University of Bielefeld[15,23] at two camera (nozzle-to-plate) distances (25 and 50 cm) with an accelerating voltage of about 60 kV. The sample used for the GED study was kept at –10 °C during the GED experiment, and the inlet system and nozzle were at room temperature. The main conditions of the GED experiment are presented in Table 6. The wavelength of electrons was determined from diffraction patterns of a benzene standard measurement under the same conditions. The molecular intensities $I_{mol}(s)$ were obtained in the s ranges 5.6–35.6 Å^{-1} and 1.9–15.5 Å^{-1} for the short and long nozzle-to-plate distance, respectively [$s = (4\pi/\lambda)\sin\theta/2$; λ is the electron wavelength and θ is the scattering angle]. The experimental [and difference (experimental – theoretical)] intensities $s^4I_{mol}(s)$ are given in Figure 11. The final R-factors are: R_G = 10.93% and R_D = 6.73%. Technical details, data reduction procedure, structure refinement programs and strategies are described in detail elsewhere (detailed information on the refinement prerequisites and results are listed in the Supporting Information: Tables S2–S8).[23]

Table 6. Conditions of the GED experiment.

Nozzle-to-plate distance / mm	500.00	250.00
Electron beam current / nA	230	180
Electron wavelength / Å	0.04830(1)	0.04839(1)
Exposure time / s	30–61	60–61
Residual gas pressure / mbar	8×10^{-6}	7×10^{-6}

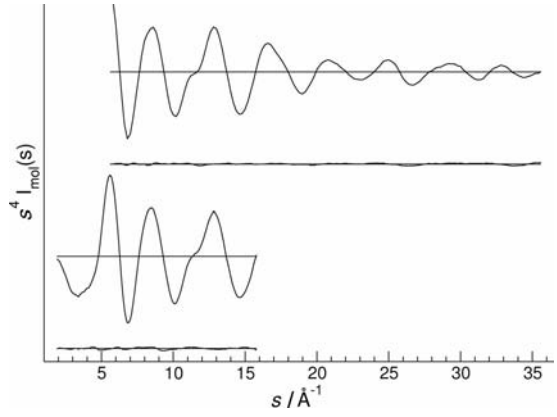

Figure 11. Experimental and difference (experimental minus theoretical) molecular scattering intensity curves for F_2PN_3.

Matrix Isolation: Gaseous F_2PN_3 was mixed with argon (1:500) in a 1-L stainless-steel storage container, and small amounts (ca. 1 mmol) of the mixture were then deposited within 30 min onto the cold matrix support (15 K, Rh plated Cu block) under high vacuum. Heating of the gaseous mixture prior to deposition was performed by forcing the gas stream through a quartz tube (i.d. 4.0 mm, at the end with a pinhole of 1 mm), which was heated at

the end over a length of ca. 15 mm with a Kantal wire (o.d. 0.25 mm). Infrared spectra of the matrix-isolated species were recorded through a CsI window on a FTIR spectrometer (IFS 66v/S Bruker) in reflectance mode by using a transfer optic. A KBr beam splitter and a MCT detector were used in the region 5000–530 cm^{-1}, and a Ge-coated 6-μm Mylar beam splitter combined with a He(l)-cooled Si bolometer in the region of 700 to 180 cm^{-1}. For each spectrum 200 scans at a resolution of 0.25 cm^{-1} were recorded. Details of the matrix-isolation apparatus are described elsewhere.[24]

NMR Spectroscopy: NMR spectra were measured on a Bruker Avance 400 spectrometer at room temperature in flame-sealed glass tubes (o.d. 4.0 mm, i.d. 3.0 mm, length 15 cm) placed in thin–walled, 5-mm NMR tubes with some CD_2Cl_2 as a lock: ^{19}F NMR (376.5 MHz), ^{31}P NMR (242.9 MHz), ^{14}N NMR (43.4 MHz), and ^{15}N NMR (60.8 MHz). The chemical shifts are referenced to external $CFCl_3$ (^{19}F), H_3PO_4 (^{31}P), and CD_3NO_2 (^{14}N and ^{15}N).

F_2PN_3: ^{19}F NMR: δ = –57.8 ppm (d), $^1J(^{31}P–^{19}F)$ = 1309 Hz. ^{31}P NMR: δ = 149.1 ppm (t). ^{14}N NMR: $\delta(F_2PNNN)$ = –279.2 ppm (s), $\Delta\nu_{1/2}$ = 247.7 Hz; $\delta(F_2PNNN)$ = –148.9 ppm (s), $\Delta\nu_{1/2}$ = 16.2 Hz; $\delta(F_2PNNN)$ = –163.8 ppm (s), $\Delta\nu_{1/2}$ = 26.6 Hz.

$F_2P^{15}NNN/F_2PNN^{15}N$: ^{15}N NMR: $\delta(F_2P^{15}NNN)$ = –279.2 ppm (m); $\delta(F_2PNN^{15}N)$ = –163.8 ppm (s), $^1J(^{15}N–^{31}P)$ = 95.4 Hz, $^2J(^{15}N–^{19}F)$ = 13.8 Hz, $^3J(^{15}N–^{31}P)$ = 8.8 Hz.

F_2PNCO: ^{19}F NMR: δ = –53.4 ppm (d), $^1J(^{31}P–^{19}F)$ = 1314 Hz. ^{31}P NMR: δ = 131.3 ppm (t). ^{13}C NMR: δ = 128.8 ppm (s).

Low-temperature NMR spectra: ^{19}F NMR spectra of the F_2PN_3 sample were also measured at low temperatures down to 183 K. These spectra did not reveal spectral changes such as line broadening relative to that recorded at 300 K or the presence of different conformers.

Vapor Pressure: The vapor pressure measurements were performed with a small sample in a container connected to a small vacuum line (total volume ca. 20 mL), equipped with a calibrated capacitance manometer (MKS Baratron, Burlington, MA, 1000 mbar absolute). In the temperature range –120 to –40 °C, the obtained vapor–pressure curve is shown in Figure S7. Pure F_2PN_3 is a colorless gas, which freezes to a glassy solid at ca. –120 °C, and the boiling point is 8 °C obtained by extrapolating the vapor–pressure curve [Equation (2)].

$$\log p = -1536.0/T + 8.343 \quad (p \text{ in mbar}, T \text{ in K}) \qquad (2)$$

Computational Details: Structural and force field calculations were performed by using the Gaussian 03 software package[25] at different DFT (B3LYP,[26] BP86,[27] MPW1PW91[28]) levels with the 6-311+G(3df) basis set, as well as the complete basis set CBS-QB3 method.[29] Local minima were confirmed by vibrational frequency analysis and transition states by intrinsic reaction coordinate (IRC) calculations.[30] Additional ab initio calculations (HF,[31] MP2,[32] CAS-MCSCF[33]) with the TZVPP[34] basis set were conducted for comparison. Natural bond orbital (NBO) analysis[35] was performed as implemented in the Gaussian 03 software package for the evaluation of donor–acceptor (bond and lone pair – antibonding) interactions in the NBO basis. Perturbative estimates of the stabilization energy E_2 associated with these NBO delocalizations[18] are expressed by [Equation (3)].

$$E_2 = \Delta E_{ij} = q_i \frac{F(i,j)^2}{\varepsilon_j - \varepsilon_i} \qquad (3)$$

where q_i is the occupancy of the ith donor orbital, ε_i and ε_j are the energies of the ith donor and the jth acceptor orbitals, and $F(i,j)$ is the (i,j) off-diagonal NBO Fock matrix element. Estimates of steric exchange repulsion energies $E(i,j)$ of individual orbital pairs (i,j) were calculated by using the $STERIC$ keyword[36] with the program GENNBO 5.0 W[37] at the B3LYP/6-311+G(3df) optimized structures. 2-D contour plots of vicinal interactions between preorthogonal PNBOs are displayed by using the program NBOView.[38]

Supporting Information (see footnote on the first page of this article): Vapor–pressure curve, spectra showing the temperature dependence of the gas-phase IR overtone bands, Raman (solid) spectra, and Ar-matrix IR spectra of F_2PN_3, Ar-matrix IR spectrum of F_2PNCO, orbital contour plots of lone pair–antibonding orbital interactions, calculated structural parameters and energies of F_2PN_3 and F_2PNCO, details of the GED structure refinement, and NBO second-order perturbation and natural steric analyses are presented.

Acknowledgments

We express our cordial thanks to Prof. Dr. F. A. Weinhold (Wisconsin) for helpful discussions on the NBO analysis, and X. Z. thanks the Alexander von Humboldt Foundation for a research grant; H. B., H. W., and N. W. M. acknowledge the support from the Deutsche Forschungsgemeinschaft and the Fonds der Chemischen Industrie. We are indebted to Prof. Dr. R. Eujen for recording the NMR spectra.

[1] a) C. Knapp, J. Passmore, *Angew. Chem. Int. Ed.* **2004**, *43*, 4834–4836; b) I. C. Tornieporth-Oetting, T. M. Klapötke, *Angew. Chem. Int. Ed. Engl.* **1995**, *34*, 511–520; c) T. M. Klapötke, A. Schulz, *Main Group Met. Chem.* **1997**, *20*, 325–338.
[2] a) H. R. Allcock in *Synthesis and Characterisations of Poly(organophosphazenes)* (Eds.: M. Gleria, R. de Jaege), Nova *Science* New York, **2004**, pp. 1–22; b) J.-P. Majoral in *Multiple Bonds and Low Coordination in Phosphorus Chemistry* (Eds.: M. Regitz, O. J. Scherer), Thieme, Stuttgart, **1990**, pp. 455–461; c) E. Niecke, D. Gudat, *Angew. Chem. Int. Ed. Engl.* **1991**, *30*, 217–237; d) G. Bertrand, J.-P. Majoral, A. Baceiredo, *Acc. Chem. Res.* **1986**, *19*, 17–23.
[3] a) A. H. Cowley, F. P. Gabbaï, G. Bertrand, C. J. Carrano, M. R. Bond, *J. Organomet. Chem.* **1995**, *493*, 95–99; b) O. J. Scherer, W. Glassel, *Chem. Ztg.* **1975**, *99*, 246.
[4] a) X. Q. Zeng, W. G. Wang, F. Y. Liu, M. F. Ge, D. X. Wang, *Eur. J. Inorg. Chem.* **2006**, 416–421; b) W. Buder, A. Z. Schmidt, *Z. Anorg. Allg. Chem.* **1975**, *415*, 263–267.
[5] E. L. Lines, L. F. Centofanti, *Inorg. Chem.* **1972**, *11*, 2269–2270.
[6] S. R. O'Neill, J. M. Shreeve, *Inorg. Chem.* **1972**, *11*, 1629–1631.
[7] X. Q. Zeng, H. Beckers, H. Willner, *Angew. Chem. Int. Ed.* **2009**, *48*, 4828–4831; *Angew. Chem.* **2009**, *121*, 4922–4925.
[8] a) B. Hoge, J. Bader, H. Beckers, Y. S. Kim, R. Eujen, H. Willner, N. Ignatiev, *Chem. Eur. J.* **2009**, *15*, 3567–3576; b) J. R. Durig, J. Xiao, *J. Mol. Struct.* **2000**, *526*, 373–389; c) E. G. Codding, C. E. Jones, R. H. Schwendeman, *Inorg. Chem.* **1974**, *13*, 178–181.
[9] a) P. E. Baskakova, A. V. Belyakov, A. Haaland, H. V. Volden, *J. Mol. Struct.* **2001**, *567*, 197–202; b) N. W. Mitzel, *J. Chem. Soc., Dalton Trans.* **1998**, 3239–3242.
[10] R. Noble-Eddy, S. L. Masters, D. W. H. Rankin, D. A. Wann, H. E. Robertson, B. Khater, J.-C. Guillemin, *Inorg. Chem.* **2009**, *48*, 8603–8612.
[11] D. W. H. Rankin, S. J. Cyvin, *J. Chem. Soc., Dalton Trans.* **1972**, 1277–1286.
[12] S. Cradock, G. S. Laurenson, D. W. H. Rankin, *J. Chem. Soc., Dalton Trans.* **1981**, 187–190.
[13] X. Q. Zeng, M. Gerken, H. Beckers, H. Willner, *Inorg. Chem.* **2010**, *49*, 3002–3010.

[14] a) N. W. Mitzel, D. W. H. Rankin, *Dalton Trans.* **2003**, 3650–3662; b) A. J. Blake, P. T. Brain, H. McNab, J. Miller, C. A. Morrison, S. Parsons, D. W. H. Rankin, H. E. Robertson, B. A. Smart, *J. Phys. Chem.* **1996**, *100*, 12280–12287; c) N. W. Mitzel, H. Schmidbaur, D. W. H. Rankin, B. A. Smart, M. Hofmann, P. v. R. Schleyer, *Inorg. Chem.* **1997**, *36*, 4360–4368; d) N. W. Mitzel, B. A. Smart, A. J. Blake, H. E. Robertson, D. W. H. Rankin, *J. Phys. Chem.* **1996**, *100*, 9339–9347.
[15] V. A. Sipachev, *THEOCHEM* **1985**, *121*, 143–151.
[16] A. H. Brittain, J. E. Smith, R. H. Schwendeman, *Inorg. Chem.* **1972**, *11*, 39–42.
[17] A. H. Brittain, J. E. Smith, P. L. Lee, K. Cohn, R. H. Schwendeman, *J. Am. Chem. Soc.* **1971**, *93*, 6772–6776.
[18] F. Weinhold, *NBO 5.0 Program Manual*, University Wisconsin, Madison, **2001**.
[19] W. Gombler, H. Willner, *J. Phys. E: Sci. Instrum.* **1987**, *20*, 1286–1288.
[20] R. G. Cavell, *J. Chem. Soc.* **1964**, 1992–1995.
[21] R. Schmutzler, *Inorg. Chem.* **1964**, *3*, 415–421.
[22] G. G. Flaskerud, K. E. Pullen, J. M. Shreeve, *Inorg. Chem.* **1969**, *8*, 728–730.
[23] a) R. J. F. Berger, M. Hoffmann, S. A. Hayes, N. W. Mitzel, *Z. Naturforsch., Teil B* **2009**, *64*, 1259–1268; b) M. Hagemann, R. J. F. Berger, S. A. Hayes, H.-G. Stammler, N. W. Mitzel, *Chem. Eur. J.* **2008**, *14*, 11027–11038.
[24] H. G. Schnöckel, H. Willner in *Infrared and Raman Spectroscopy, Methods and Applications* (Ed.: B. Schrader), VCH, Weinheim, **1994**.
[25] M. J. Frisch, G. W. Trucks, H. B. Schlegel, G. E. Scuseria, M. A. Robb, J. R. Cheeseman, J. A. Montgomery Jr., T. Vreven, K. N. Kudin, J. C. Burant, J. M. Millam, S. S. Iyengar, J. Tomasi, V. Barone, B. Mennucci, M. Cossi, G. Scalmani, N. Rega, G. A. Petersson, H. Nakatsuji, M. Hada, M. Ehara, K. Toyota, R. Fukuda, J. Hasegawa, M. Ishida, T. Nakajima, Y. Honda, O. Kitao, H. Nakai, M. Klene, X. Li, J. E. Knox, H. P. Hratchian, J. B. Cross, C. Adamo, J. Jaramillo, R. Gomperts, R. E. Stratmann, O. Yazyev, A. J. Austin, R. Cammi, C. Pomelli, J. W. Ochterski, P. Y. Ayala, K. Morokuma, G. A. Voth, P. Salvador, J. J. Dannenberg, V. G. Zakrzewski, S. Dapprich, A. D. Daniels, M. C. Strain, O. Farkas, D. K. Malick, A. D. Rabuck, K. Raghavachari, J. B. Foresman, J. V. Ortiz, Q. Cui, A. G. Baboul, S. Clifford, J. Cioslowski, B. B. Stefanov, G. Liu, A. Liashenko, P. Piskorz, I. Komaromi, R. L. Martin, D. J. Fox, T. Keith, M. A. Al-Laham, C. Y. Peng, A. Nanayakkara, M. Challacombe, P. M. W. Gill, B. Johnson, W. Chen, M. W. Wong, C. Gonzalez, J. A. Pople, *Gaussian 03*, Revision D.01, Gaussian, Inc., Pittsburgh PA, **2003**.
[26] A. D. Becke, *J. Chem. Phys.* **1993**, *98*, 5648–5652.
[27] J. P. Perdew, *Phys. Rev. B* **1986**, *33*, 8822–8824.
[28] C. Adamo, V. Barone, *J. Chem. Phys.* **1998**, *108*, 664–675.
[29] J. A. Montgomery Jr., M. J. Frisch, J. W. Ochterski, G. A. Petersson, *J. Chem. Phys.* **2000**, *112*, 6532–6542.
[30] a) C. Gonzalez, H. B. Schlegel, *J. Chem. Phys.* **1989**, *90*, 2154–2161; b) C. Gonzalez, H. B. Schlegel, *J. Phys. Chem.* **1990**, *94*, 5523–5527.
[31] C. C. J. Roothaan, *Rev. Mod. Phys.* **1951**, *23*, 69–89.
[32] C. Møller, M. S. Plesset, *Phys. Rev.* **1934**, *46*, 618–622.
[33] The GAMESS (ref.[33a]) program package (Version April, 11 **2008**) was used for the MCSCF(ref.[33b]) calculations with the CAS scheme (ref.[33c]): a) M. W. Schmidt, K. K. Baldridge, J. A. Boatz, S. T. Elbert, M. S. Gordon, J. J. Jensen, S. Koseki, N. Matsunaga, K. A. Nguyen, S. Su, T. L. Windus, M. Dupuis, J. A. Montgomery, *J. Comput. Chem.* **1993**, *14*, 1347–1363; b) M. R. Hoffman, D. J. Fox, J. F. Gaw, Y. Osamura, Y. Yamauchi, R. S. Grev, G. Fitzgerald, H. F. Schaefer, P. J. Knowles, N. C. Handy, *J. Chem. Phys.* **1984**, *80*, 2660–2668; c) B. O. Roos in *Advances in Chemical Physics: Ab initio Methodsin Quantum Chemistry, Part II* (Eds.: K. P. Lawley), John Wiley & Sons Ltd., Chichester, England, **1987**, ch. 69, p. 399.
[34] N. Godbout, D. R. Salahub, J. Andzelm, E. Wimmer, *Can. J. Chem.* **1992**, *70*, 560–571.
[35] A. E. Reed, L. A. Curtiss, F. Weinhold, *Chem. Rev.* **1988**, *88*, 899–926.
[36] a) J. K. Badenhoop, F. Weinhold, *J. Chem. Phys.* **1997**, *107*, 5406–5421l; b) J. K. Badenhoop, F. Weinhold, *Int. J. Quantum Chem.* **1999**, *72*, 269–280.
[37] E. D. Glendening, J. K. Badenhoop, A. E. Reed, J. E. Carpenter, J. A. Bohmann, C. M. Morales, F. Weinhold, *NBO 5.0*, University of Wisconsin, Madison, **2001**, www.chem.wisc.edu/~nbo5.
[38] M. Wendt, F. Weinhold, *NBOView 1.1: NBO Orbital Graphics*, University Wisconsin, Madison, **2001**.

Received: August 18, 2010
Published Online: November 2, 2010

